A Discrete and Distributed Steady Blowing Application on a High Reynolds Number Semispan Supercritical Wing Configuration (Invited)

Gregory S. Jones[1], William E. Milholen, II[2], David T. Chan[3], Scott L. Goodliff[4], C. Mark Cagle[5], Jared S. Fell[6]

NASA Langley Research Center, Hampton, VA, 23681

The FAST-MAC circulation control model was modified to test an array of steady and unsteady actuators at realistic flight Reynolds numbers in the National Transonic Facility at the NASA Langley Research Center. Previous experiments in the FAST-MAC test series used a fullspan tapered slot, and that configuration is used as a baseline for performance and weight flow requirements. The goal of the latest experiment was to reduce the weight flow required to achieve comparable performance established by the baseline FAST-MAC data. Thirty-nine interchangeable actuator cartridges of various designs were mounted into the FAST-MAC model where the exiting jet was directed over a 15% chord simple hinged-flap. These two types of actuators were fabricated using rapid prototype techniques and their design performance was optimized for a transonic cruise configuration having a 0° flap deflection. The steady actuators were found to provide an off-design drag reduction of 5.5%, nearly equaling the drag reduction of the fullspan tapered slot configuration, but with a 69% weight flow reduction. This weight flow savings is similar to the sweeping jet actuators, but with better drag performance.

Nomenclature

AR	=	aspect ratio
b	=	wing span (in)
CFD	=	Computational Fluid Dynamics
C_p	=	pressure coefficient
c	=	chord (in)
C_{DIS}	=	nozzle discharge coefficient
ctg.	=	actuator cartridge
C_μ	=	steady momentum coefficient
$\bar{C}_\mu$	=	average momentum coefficient sweeping jet at jet exit
h	=	actuator throat exit height (in)
MAC, $\bar{c}$	=	mean aerodynamic chord
MPA	=	model preparation area
MCV	=	multiple critical venturi
M_∞	=	wind tunnel Mach number
NPR	=	nozzle pressure ratio ($P_{o(J)}/P_\infty$)
OML	=	outer mold line
$P_{o(J)}$	=	jet total pressure (psi)
$P_{o(THROAT)}$	=	throat total pressure (psi)
P_∞	=	wind tunnel static pressure (psi)
q_∞	=	freestream dynamic pressure (psf)
Re_c	=	chord Reynolds number
S	=	wing plan form area (ft^2)
SPL	=	sound pressure level (decibels, dB)
SMSS	=	Sidewall Model Support System
t/c	=	wing thickness to chord ratio
T_O	=	wind tunnel total temperature (°R)
$T_{O\,(JET)}$	=	jet total temperature (°R)
U_∞	=	free stream velocity (ft/sec)
U_{JET}	=	throat jet velocity for steady blowing (ft/sec)
$U_{EXIT\text{-}SJ}$	=	average sweeping jet exit velocity (ft/sec)
$U_{EXIT\,(HW)}$	=	exit velocity, hot-wire (ft/sec)
U_{THROAT}	=	throat velocity (ft/sec)
USM3D	=	Unstructured Mesh 3D Navier-Stokes flow solver
w_I	=	ideal weight flow (lbm/sec)
w_M	=	measured weight flow (lbm/sec)
X, Y, Z	=	orthogonal measurement location (in)
y	=	actuator throat width (in)
α	=	angle of attack (degrees)
η	=	span location/b
λ	=	wing taper ratio
Λ_{LE}	=	leading edge sweep angle (degrees)
ρ_∞	=	free stream density (lbm/ft^3)
ρ_{JET}	=	jet density (lbm/ft^3)

[1] Research Engineer, Configuration Aerodynamics Branch, Mail Stop 267, AIAA Associate Fellow
[2] Research Engineer, Configuration Aerodynamics Branch, Mail Stop 499, AIAA Senior Member
[3] Research Engineer, Configuration Aerodynamics Branch, Mail Stop 499, AIAA Senior Member
[4] Test Engineer, Jacobs Technology, Inc., Mail Stop 267
[5] Designer, Aeronautics Systems Engineering Branch, Mail Stop 238
[6] Designer, Aeronautics Systems Engineering Branch, Mail Stop 238

Introduction

The study of circulation control has a long history,[1,2,3,4,5] but it has not been applied to commercial aircraft due to system requirements that include the air source (i.e., engine bleed), design complexity, weight penalties, engine-out conditions, etc. Application of these blowing systems to takeoff and landing configurations have been demonstrated in a laboratory environment for boundary layer separation management, and improved aerodynamic performance. However, those benefits have not crossed the cost/benefit threshold for this technology to buy its way onto an aircraft for the high-lift applications alone. It is thought that the combined improvements in the high-lift and cruise performance would be enough to overcome the barriers to its application to commercial aircraft. Therefore, the realization of improved cruise efficiency at realistic flight conditions potentially changes the paradigm for circulation control applications.

One of the major challenges to the application of circulation control to commercial aviation is related to the amount of bleed air that will be required of the propulsion system to achieve the comparable performance of state-of-the-art high-lift systems. Recent efforts using sweeping jets to reduce the weight flow requirements is highlighted in references 6, 7, and 8. While the application of sweeping jets to replace conventional high-lift systems is promising, the noise generated by the jets is a potential obstacle to implementation. The intent of the latest test series was to achieve improved flight performance of a vehicle using active flow control with minimal bleed requirements by reducing the weight flow requirements established with the fullspan steady blowing. This was demonstrated on the semispan Fundamental Aerodynamic Subsonic Transonic-Modular Active Flow (FAST-MAC) model shown in Figure 1 by modifying the blowing configuration to accept alternative blowing cartridges. This paper will focus on the application of active flow control using distributed steady and unsteady jets (Figure 2) to a commercial aircraft cruise configuration.

Background

The circulation control methods that will be discussed throughout this paper center around momentum introduced directly to the near-wall region via a blowing slot, located near the wing trailing edge, and directed over a simple short-chord hinged-flap as shown in Figure 3. For steady circulation control applications, the flow is typically characterized by jet momentum (C_μ) or nozzle pressure ratio (*NPR*) that defines the jet velocity (U_{THROAT}) at the minimum area along the flow path. The minimum area is located at the jet exit for the fullspan steady blowing configuration and upstream of the exit for the distributed steady and unsteady actuators as shown in Figure 2. The jet momentum is generally related to ideal conditions as shown in Equation 1, where internal boundary layer growth is ignored and weight flow is a function of the total pressure measured in the settling chamber of the aft plenum. The jet momentum can also be characterized by using the measured weight flow and the nozzle discharge coefficient as shown in Equation 2. The average jet velocity used in Equations 1 and 2 assumes that the flow expands isentropically to the freestream static pressure and is characterized by the *NPR* and jet temperature ($T_{O(JET)}$) shown in Equation 3. Figure 2 shows a schematic of a sweeping jet actuator that creates a self-sustaining oscillating jet due to the feedback tubes alternating the direction of the internal flow path direction in the nozzle. The external velocity field of the sweeping jet is time-dependent making it difficult to measure when using a point measurement system. For these reasons, the calculation of a momentum coefficient for the sweeping jet was modified, using an average exit velocity (Equation 4) instead of the throat.

The performance that is measured by the balance is correlated to the averaged C_μ at the exit of the nozzle. However, the measured *NPR* and jet velocity are based on the nozzle throat characteristics that complicates the definition of U_{EXIT} used in the calculation of C_μ for the two actuators used in this test series. The values used for $U_{EXIT\text{-}SJ}$ will be based on the ratio of the measured average hot-wire velocity across the exit of a single actuator, and the throat velocity of the actuator in quiescent conditions shown in Figure 4.

$$C_\mu = \frac{\text{THRUST}}{q_\infty S} = \frac{2hy}{\bar{c}b}\frac{\rho_{JET}}{\rho_\infty}\frac{U_{JET}^2}{U_\infty^2} \quad (1)$$

$$C_\mu = \frac{W_M\, U_{EXIT}}{q_\infty\, S} = \frac{C_{DIS}\, W_I\, U_{EXIT}}{q_\infty\, S} \quad (2)$$

$$U_{THROAT} = \sqrt{\frac{2\gamma R T_{O(JET)}}{\gamma - 1}\left[1 - \left(\frac{1}{NPR}\right)^{\frac{\gamma-1}{\gamma}}\right]} \quad (3)$$

$$U_{EXIT-SJ} = U_{THROAT}\left(\frac{U_{EXIT\,(HW)}}{U_{THROAT}}\right) \quad (4)$$

$$NPR = \frac{P_{o(THROAT)}}{P_\infty} \quad (5)$$

Experimental Setup

Wind Tunnel

The FAST-MAC model used an advanced circulation control high-lift and cruise system that has been tested multiple times in the NASA Langley National Transonic Facility (NTF) utilizing a facility air delivery system. The NTF[9] (Figure 5) is one of a limited number of wind tunnel facilities that can achieve flight Reynolds numbers and Mach numbers for transport-aircraft at both cruise and high-lift operations. The tunnel is a fan-driven, closed-circuit, continuous-flow, pressurized wind tunnel capable of operating either in dry air at warm temperatures or in nitrogen gas from warm to cryogenic temperatures. The test section is 8.2 ft by 8.2 ft in cross section and 25 ft in length. The test section floor and ceiling are slotted (6 percent open), and the sidewalls are solid. The wind tunnel is capable of an absolute pressure range from 1 atmosphere to 8.3 atmospheres, a temperature range from -270°F to 130°F, a Mach number range from 0.1 to 1.2, and a maximum Reynolds number of 146×10^6 per foot at Mach 1. For the circulation control test described in this paper, the temperature envelope was limited to -50°F to 120°F due to limitations of the air delivery and model protection systems.

FAST-MAC Model

The FAST-MAC model shown in Figure 6 is based on a supercritical wing that was designed to become an NTF standard for evaluating performance characteristics of integrated active flow control and propulsion systems. The modular design and construction of the FAST-MAC model provides a capability of changing the leading edge, trailing edge, upper skin geometry (with or without engine simulators), and active or passive flow control technology. The outer mold line (OML) of the model was optimized for a cruise Mach number of 0.85 and a lift coefficient of 0.50 at a Reynolds number based on mean aerodynamic chord of 30×10^6. The design utilized an unstructured Navier-Stokes flow solver USM3D[10] in conjunction with the CDISC design code.[11] The CDISC design method is highly efficient because the geometry changes are introduced in a manner that allows both the geometry and the simulated aerodynamic analysis to converge in unison. The flow was assumed to be fully turbulent, and a wall-function version of the Spalart-Allmaras turbulence model was employed. A tangential blowing slot was added at the 85%-chord location on the upper surface, and it was directed over a 15%-chord simple-hinged flap for both the cruise and high-lift modes.

Figure 7 shows the cutaway view of the FAST-MAC semispan model geometry. The wing has an aspect ratio of 5.0, taper ratio of 0.40, leading edge sweep of 30°, and no dihedral. The chord length at the side of the fuselage is 25.0 inches, resulting in a mean aerodynamic chord of 19.4 inches. The generic fuselage is comprised of circular cross sections with a maximum width of 4.0 inches. The wing is mounted in the midfuselage position to simplify the routing of the high-pressure air supply lines. To reduce wall boundary layer effects, the model was offset from the tunnel sidewall using a 2.0-inch nonmetric standoff,[12] which has a profile shape identical to that of the fuselage centerline.

The model was designed to operate at the maximum pressure limits of the facility and a temperature range of -50°F to 120°F. While a typical NTF wind tunnel model such as the FAST-MAC accurately characterizes outer mold lines of an advanced high Reynolds number wing model, the internal flow paths are only representative at the jet exit. High dynamic pressures are generally required to achieve high Reynolds number conditions for a typical semispan NTF model as shown in Figure 8. As such, the high model loading and resulting high model stresses limited accurate internal flow path geometries due to strength of materials and limited volume within the NTF FAST-MAC model.

Air Delivery System

The dual flow air delivery system[13] is a high-pressure air system that provides a continuous source of clean, dry air to the test article through the Sidewall Model Support System (SMSS). The FAST-MAC model utilized only the high-flow leg of this system as shown in the schematic in Figure 9, and it is equipped with coarse and fine control valves that can provide flow rates up to 23 lbm/sec. The system has a multiple critical venturi (MCV) system located outside the tunnel plenum to measure the total weight flow. The total temperature of the model air stream can be set from 20°F to 120°F by using a steam heating system. The FAST-MAC model was designed to enable the flow to be tailored along the span by independently controlling the flow through any combination of the four flow paths distributed along the span of the wing. The challenge for this test was the ability to set the very low flow rates by balancing the *NPR* settings with the model valves while using the fine flow control valve and the smallest venturi in the MCV. The jet exit total pressure parameters used in the calculation of the throat velocity and C_μ have measurement

uncertainties that are less than ±0.1% of reading for the range of flow conditions tested. The weight flow measured in the NTF air station by the MCV system has an uncertainty of ±0.35% of reading.[14]

Balance System

The NTF-117S is a 5-component force and moment balance that is mounted inside the SMSS as shown in Figure 10. The SMSS provides a heated enclosure that maintains a stable temperature for the balance and the pitch mechanisms. The balance characteristics are highlighted in Table 1.

The Pressure Interface Piece (PIP) is the metric-to-nonmetric bridge that delivers high-pressure air to the model. The entire SMSS/balance/air system was calibrated to determine the pressurization and temperature effects of the PIP on the balance measurements. The calibration included the range of pressures needed for this sweeping jet test series. Those pressure tares are subtracted from the balance data to obtain pure aerodynamic loads.[15, 16] Recent improvements in the balance temperature control and other SMSS modifications resulted in a transonic 2-sigma drag repeatability of ±3 counts.[17, 18] Those improvements were necessary to meet the requirements for this sweeping jet study due to the small blowing effects associated with the separation control region of the FAST-MAC high-lift system and the cruise drag benefits in the range of Mach 0.85 to 0.88.

Thrust Removal

For propulsion simulation or testing that involves blowing concepts, the force and moment data acquired from a strain gauge balance frequently include the effects of the static thrust from the nozzle. In the cases where the thrust is metric (i.e. sensed and measured by the balance), the effect of the static thrust needs to be removed from the wind-on balance measurements to isolate the pure aerodynamic and jet-induced effects in the force and moment data. The data shown in this report will focus on the pure aerodynamic effects (i.e., the thrust has been removed). The procedure for this thrust removal is described in Reference 19. To augment the thrust removal and weight flow through each flow path a calibrated nozzle system shown in Figure 11 was developed. Preliminary weight results from this system were promising, however the nozzle areas were not matched with the FAST-MAC throat areas resulting in a modification to the calibrator system that was not implemented due to schedule.

Distributed Actuators

Thirty-nine interchangeable steady and/or sweeping jet actuators were options for installations in the NTF FAST-MAC model. The actuators are integrated into the wing using a cartridge design shown in Figure 12 where each individual actuator can be replaced in the aft plenum cover without requiring a major model change. The exit height of both actuator designs correspond to a constant *h/c* of 0.0021 used in the baseline fullspan steady blowing configuration. This resulted in a slot height variation of the cartridges along the span to maintain that specification. Unfortunately, fabrication limitations restricted the wall thickness of the outboard actuators to a constant height of 0.040 inches, resulting in flow paths three and four having a varying *h/c* as shown in Table 2. While the exit height was the same for both actuators the steady actuator has a 20% larger exit area than the sweeping jet actuator and a 62% larger throat area.

The two actuator configurations (shown in Figure 2) were optimized based on the actuator authority, which is defined by the velocity of the jet distributed across the flap. The steady actuator has a total sweep angle of $\theta = \pm 16°$, while the sweeping jet actuator has a sweep angle of $\theta = \pm 35.5°$. The cartridges were fabricated using a plastic stereolithography apparatus (SLA) rapid prototyping technique. It was determined that the manufacturing tolerance of the SLA sweeping jet actuators could be maintained to within ±0.001 inch. That equated to ±2.5% of the smallest throat dimension to be used in the FAST-MAC model. To verify that the cold environment of the tunnel would not visibly alter the geometry of the plastic SLA actuator cartridges, a frequency test was performed in a cryogenic test chamber at 3 times the expected pressure.

Hot-wire Data Acquisition

While it was desired to perform hot-wire surveys while the model was in the test section, no hot-wire data were acquired due to cost and schedule. The model was moved to the NTF Model Prep Area (MPA) where the surveys were completed. Prior to the surveys the hot-wire system was calibrated over the estimated range of the actuator flow parameters. An example of a hot-wire calibration is shown in Figure 13. The calibration was divided into three ranges

to keep the percent reading error less than ±1%. A block diagram of the data acquisition system is highlighted in Figure 14. Acquisition on the high-speed data system acquired data at 102.4k samples per second which satisfied a Nyquist criteria of 50 kHz. The hot-wire was mounted vertically and zeroed with the lower prong at the surface of the flap as shown in Figure 15. The first pass of the survey was 0.025 inches downstream of the actuator exit and the reference prong of the hot-wire was maintained at ΔZ of +0.002 inches from the flap surface. The *X*-*Y*-*Z* stepper motor positioning system has a resolution of ±0.0004 inches for the *X* and *Y* axis and ±0.00004 for the *Z* axis.

Actuators in Quiescent Flow

The overall performance of the active flow control systems being evaluated in this paper can be correlated to the efficiency of the actuators being tested. To gain an understanding of the actuator performance hot-wire surveys were obtained at four downstream planes relative to the jet exit in quiescent air. Figure 16 features the streamwise hot-wire measurement locations downstream of the actuator jet exit where the spanwise step size ΔY is 0.10 inches. These data can be correlated to the surface oil flow visualization shown in the same figure.

The efficiency of each of the actuator systems will be defined by the actuator authority (i.e. jet magnitude) and coverage onto the upper surface of the flap as a function of *NPR*. The interactions of ajacent steady actuators in quiescent air are highlighted with a CFD solution shown in Figure 17 for an *NPR*=3.0. The contrast of the two actuator configurations is highlighted by the time-averaged velocity profiles that are derived from the Probability Density Function (PDF) data at each location. This is illustrated in Figure 18 and 19 for a single sweeping jet at the exit plane for different span locations of the actuator and Figure 20 for the steady actuator at different streamwise locations. While the peak velocity approaches sonic conditions for the sweeping jet, the average is biased by the minimum velocity that occurs when the jet sweeps away from the measured location.

Since the *NPR* is based on the throat conditions, the magnitude of the jet velocity at the nozzle exit plane of the actuator is a function of the actuator jet diffuser. In general, the jet velocity is uniform at the exit plane of the steady actuator. The exception is the near-field wakes of the internal splitter plates of the steady actuator as shown in Figure 21. The wakes of these splitter plates seem to propagate downstream (see oil flow visualization in Figure 16) and interact with the adjacent actuator flow fields. There also appears to be a three-dimensional rollup of the flow in the gaps between the actuators that is supported with the hot-wire data in Figure 21. While the single sensor hot-wire is unable to resolve flow angle, it's spectra shown in Figure 22 can be used with the profile data of Figure 21 to characterize mixing and the expansion of the jet as it moves downstream.

Likewise, the sweeping jet velocity is not uniformly distributed at the exit[20] due to the diamond splitter as shown from hot-wire measurements in Figure 23. While the peak velocities of the sweeping jet actuators are comparable to the steady jet actuators the overall authority or average velocity of the sweeping jet actuators on the flap is approximately 50% of the steady jet actuators. This is determined by comparing the exit profile data in Figures 21 and 23.

The sweeping jet velocity spectra shown in Figure 24 highlights a two order-of-magnitude shift in the low frequency turbulence as the jet propagates downstream. This occurs as the primary sweeping frequency decays approximately one order-of-magnitude. The primary sweeping frequency of 1.33kHz is approximately five orders-of-magnitude greater than the broadband velocity characteristic of the steady jet actuator at the jet exit. The velocity exiting the sweeping jet actuator has an associated Sound Pressure Level (SPL) that varies with *NPR* as shown in Figure 25. The sweeping jet has a SPL that is 35 dB larger than the steady actuator.

Performance Results

The analysis of the repeat runs for this test indicated that the 2σ variation of the drag coefficient was $C_D = \pm 0.0003$ for the discussion presented below.

Steady Slot Blowing

The transonic steady slot blowing results obtained during the third test of the FAST-MAC model is described in Reference 21 and 22 and focuses on evaluating numerous upgrades to the force and moment measurement system. These upgrades were aimed at improving the transonic drag repeatability at the mild cryogenic condition of -50°F. The model was configured with a fullspan nondimensional slot height of $h/c = 0.0021$ for that test.

The effect of the steady blowing on the wing pressures at an off-design Mach number of 0.88 are shown in Figure 26 at $\alpha = 3°$ and $Re_c = 30 \times 10^6$. The nonblowing result, $NPR = 1.00$, indicates shock-induced flow separation on the outboard portion of the wing. The addition of blowing, $NPR = 1.80$, strongly influenced the wing pressures, suggesting the flow has reattached downstream of the shockwave. Blowing also caused the shock to move aft 5% chord at $\eta = 0.60$, and 10% of chord at $\eta = 0.80$, with little change in the shock strength. Figure 27 shows the effect of the steady blowing on the measured lift and drag coefficients. At the design lift coefficient of 0.50, the drag was reduced by 6.5% (0.0025 or 25 counts) for $NPR = 1.78$ and $C_\mu = 0.0049$.

Sweeping Jet Actuators

Figure 28 presents the effect of the sweeping jet actuator at the off-design condition of $M = 0.88$, $\alpha = 3°$, and $Re_c = 15 \times 10^6$. The nonblowing case ($NPR = 1.00$) again suggests shock-induced flow separation on the outboard portion of the wing ($\eta = 0.80$). The activation of the sweeping jets (with $NPR = 3.97$) have a noticeable effect on the wing pressures. At $\eta = 0.60$ the shock has moved aft slightly, and the downstream pressure recovery has improved. At the outboard station ($\eta = 0.80$), the shockwave has moved aft approximately 5% chord, while the downstream pressure recovery still indicates flow separation. As with the steady blowing case, the shockwave strength has not been altered. Even though further research is necessary to appreciate the level of flow reattachment that may have occurred, the drag polar comparison in Figure 29 indicates that the sweeping jets have reduced the drag coefficient by 3.3% (0.0014 or 14 counts). Although the sweeping jets offer half the drag reduction shown for the steady blowing case (Figure 29), the sweeping jets accomplished this with an 80% reduction in weight flow.

Steady Jet Actuators

Figure 30 examines the effect of the discrete steady actuators on the outboard wing pressures at the off-design condition of Mach 0.88, $\alpha = 3°$, and $Re_c = 15 \times 10^6$. The blowing case illustrated here, $NPR = 4.22$, was found to be in close agreement with the steady slot blowing wing pressures. At the $\eta = 0.60$ station, the shock has moved aft 5% chord and the pressure recovery at the trailing edge has been altered. At the outboard station the shock moved aft 10%, and the pressure recovery again suggests the flow has reattached downstream of the shockwave. This performance is in sharp contrast to what was obtained with the sweeping jet actuator, but at the cost of increased weight flow. The effect of the steady blowing actuators on the measured lift and drag coefficients are presented in Figure 31. At the design lift coefficient of 0.50, the drag was reduced by 5.5% (0.0023 or 23 counts) for $NPR = 3.98$.

The effect of varying spanwise blowing was examined by turning off the two inboard plenums for the same off-design condition. Although the two inboard rows of wing pressures were not presented above, the attached flow over this portion of the wing appeared to have minimal response to the steady blowing actuators. Figure 32 compares the wing pressures for the outboard blowing case to the above configuration having all steady actuators active. The wing pressures are nearly identical, and the outboard blowing case provides a significant 45% reduction in C_μ, which corresponds to a 48% reduction in required weight flow.

Figure 33 compares the wing pressures for both discrete steady blowing cartridge configurations to the open slot case for the same off-design condition. The pressure distributions are very similar. At the $\eta = 0.60$ station, the blown slot configuration moves the shock aft 5% chord, but the downstream pressure recovery is nearly identical. At the $\eta = 0.80$ station, the shock location is identical for all three cases, with some minor variations in the downstream pressure recovery. The performance of the discrete steady actuators is indeed encouraging. Significant weight flow reductions with respect to the slot blowing case are: 41% for all steady cartridges active, and 69% for outboard steady cartridges active. The latter weight flow savings rivals that obtained with the less effective sweeping jet actuators.

Concluding Remarks

The success of active flow control applied to transonic cruise applications has been demonstrated using three blowing configurations using the NASA FAST-MAC model tested in the NTF. The goal of reducing the weight flow requirements over the classic fullspan blowing configuration has been achieved with a distributed sweeping jet configuration and a distributed steady blowing configuration. While the sweeping jet actuator showed the most reduction in weight flow of 80% compared to the fullspan baseline configuration, the steady actuator provided a weight flow reduction of 41%. However, activating only the outboard steady actuators was comparable to the performance of the fullspan steady actuators and fullspan steady baseline configuration. The partial span steady actuator configuration resulted in a 69% reduction in weight flow at a comparable *NPR* of 3.98. This was 11% more than the sweeping jet actuator, but did achieve a drag benefit of 5.5% compared to the 3.3% improvement of the sweeping jet configuration. These benefits of the steady actuator can be related to the jet exit velocity profiles of the distributed actuator configurations. Each of the distributed actuator configurations were evaluated in a quiescent environment to assess the blowing authority. While the steady actuator configuration required more weight flow for a given *NPR* compared to the sweeping jet actuator it did provide an additional 9 count cruise drag benefit. An added benefit of the steady jet actuator is that the SPL 35 dB lower than the sweeping jet actuator. The cruise drag reduction benefits coupled with the high-lift benefits of both distributed actuator systems evaluated here, warrant an aircraft systems evaluation that increase the potential for active flow circulation control to be applied to the next generation vehicle.

Acknowledgements

This experimental effort has been supported by the Advanced Air Transport Technology (AATT) project within the NASA Aeronautic Research Mission Directorate program. Special thanks are given to Ruben Del Rosario, Rich Wahls, Scott Anders, Sally Viken, Susan Wilz, and Latunia Melton for their support and latitude in the design and testing during this phase of the FAST-MAC effort. Sincere gratitude is given to Rob Andrews for the actuator rapid prototyping that resulted in multiple configurations that were tested. The successful testing of all four phases of the FAST-MAC effort could not have been accomplished without the dedication, technical expertise, and energy of the entire NTF staff led by Don Saxer and Roman Paryz. Special recognition is given to Jim O'Shaughnessy, Roy Armstrong and Ron Rauschenbach for the development of the actuator installation techniques that proved to be the cornerstone of this successful test series.

Table 1. NTF SMSS Balance Loads.

Component	NTF 117S
Normal Force lbs (N)	12,000 (53,379)
Axial Force lbs (N)	1,800 (8,007)
Pitching Moment lbs-in (N-m)	90,000 (10,169)
Rolling Moment lbs-in (N-m)	669,000 (7,558)
Yawing Moment lbs-in (N-m)	100,350 (11,338)

Table 2. Actuator dimensions.

			STEADY ACTUATOR			SWEEPING JET ACTUATOR		
Actuator	Actuator Y-Center (inches)	h/c	SPACING = ΔCENTER/ EXIT WIDTH	INDIVIDUAL THROAT AREA (in^2)	INDIVIDUAL EXIT AREA (in^2)	SPACING = ΔCENTER/ EXIT WIDTH	INDIVIDUAL THROAT AREA (in^2)	INDIVIDUAL EXIT AREA (in^2)
1-2	1.84	0.0029	-	0.0228	0.0590	-	0.0154	0.0504
1-3	3.33	0.0028	1.6257	0.0227	0.0586	1.8030	0.0154	0.0493
1-4	4.45	0.0028	1.2295	0.0227	0.0572	1.3636	0.0154	0.0481
1-5	5.89	0.0028	1.5770	0.0226	0.0551	1.7491	0.0154	0.0470
1-6	7.02	0.0028	1.2295	0.0226	0.0538	1.3636	0.0154	0.0459
1-7	8.55	0.0028	1.6678	0.0222	0.0524	1.8724	0.0150	0.0442
1-8	9.67	0.0028	1.2633	0.0217	0.0511	1.4151	0.0143	0.0422
2-1	11.47	0.0028	2.2027	0.0170	0.0439	2.6150	0.0107	0.0354
2-2	12.83	0.0027	1.6736	0.0170	0.0427	1.9869	0.0107	0.0345
2-3	14.20	0.0027	1.6724	0.0169	0.0414	1.9854	0.0107	0.0335
2-4	15.42	0.0027	1.5385	0.0169	0.0402	1.7817	0.0107	0.0325
2-5	16.76	0.0027	1.7568	0.0168	0.0390	1.9578	0.0107	0.0315
2-6	18.01	0.0026	1.6644	0.0163	0.0378	1.8662	0.0100	0.0295
2-7	19.33	0.0026	1.8425	0.0156	0.0365	2.0638	0.0094	0.0276
2-8	20.74	0.0026	2.0195	0.0151	0.0353	2.2605	0.0088	0.0258
3-1	22.27	0.0026	2.5667	0.0110	0.0251	2.8814	0.0064	0.0212
3-2	23.09	0.0026	1.4156	0.0112	0.0245	1.5556	0.0064	0.0208
3-3	23.92	0.0025	1.4156	0.0111	0.0239	1.5556	0.0064	0.0203
3-4	24.99	0.0025	1.8680	0.0111	0.0234	2.0207	0.0064	0.0198
3-5	25.74	0.0025	1.3128	0.0111	0.0228	1.4124	0.0064	0.0193
3-6	26.49	0.0025	1.2807	0.0110	0.0222	1.4124	0.0064	0.0188
3-7	27.56	0.0025	1.8204	0.0110	0.0222	2.0075	0.0064	0.0188
3-8	28.31	0.0026	1.2807	0.0110	0.0222	1.4124	0.0064	0.0188
3-9	29.06	0.0026	1.2807	0.0110	0.0222	1.4124	0.0064	0.0188
3-10	30.13	0.0027	1.8340	0.0110	0.0222	2.0226	0.0064	0.0188
3-11	30.96	0.0027	1.4156	0.0110	0.0222	1.5612	0.0064	0.0188
3-12	31.79	0.0028	1.4156	0.0110	0.0222	1.5612	0.0064	0.0188
4-1	33.19	0.0029	2.3941	0.0110	0.0222	2.6403	0.0064	0.0188
4-2	34.02	0.0029	1.4105	0.0110	0.0222	1.5556	0.0064	0.0188
4-3	34.85	0.0030	1.4105	0.0110	0.0222	1.5556	0.0064	0.0188
4-4	35.92	0.0031	1.8289	0.0110	0.0222	2.0169	0.0064	0.0188
4-5	36.67	0.0031	1.2807	0.0110	0.0222	1.4124	0.0064	0.0188
4-6	37.42	0.0032	1.2807	0.0110	0.0222	1.4124	0.0064	0.0188
4-7	38.49	0.0033	1.8255	0.0110	0.0222	2.0132	0.0064	0.0188
4-8	39.24	0.0033	1.2807	0.0110	0.0222	1.4124	0.0064	0.0188
4-9	39.99	0.0034	1.2807	0.0110	0.0222	1.4124	0.0064	0.0188
4-10	41.06	0.0035	1.8357	0.0110	0.0222	2.0245	0.0064	0.0188
4-11	41.88	0.0036	1.4003	0.0110	0.0222	1.5443	0.0064	0.0188
4-12	42.70	0.0037	1.4003	0.0110	0.0222	1.5443	0.0064	0.0188

	TOTAL THROAT AREA (A)	TOTAL EXIT AREA (A)	TOTAL THROAT AREA (AA)	TOTAL EXIT AREA (AA)	AVERAGE h/c
	0.5536	1.2457	0.3417	1.0357	0.00285
FLOW PATH 1	0.1573	0.3871	0.1065	0.3270	0.00281
FLOW PATH 2	0.1316	0.3171	0.0816	0.2502	0.00268
FLOW PATH 3	0.1326	0.2751	0.0768	0.2329	0.00259
FLOW PATH 4	0.1321	0.2664	0.0768	0.2256	0.00323

Figures

Figure 1. The semispan FAST-MAC model installed in the NTF test section.

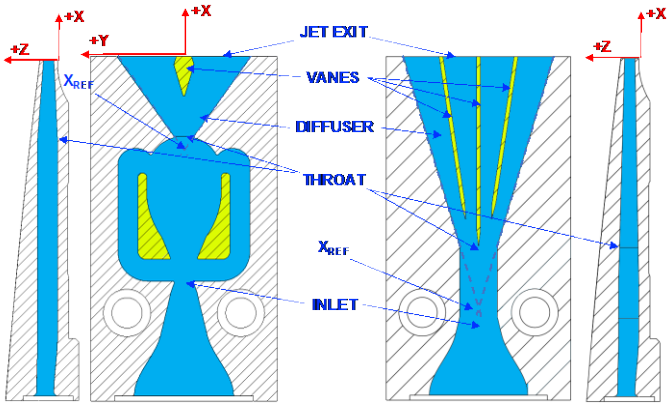

Throat: 0.080”x0.080” Sweeping Jet Cartridge **Throat: 0.150”x0.073” Steady Jet Cartridge**

Figure 2. FAST-MAC actuator cartridge geometries.

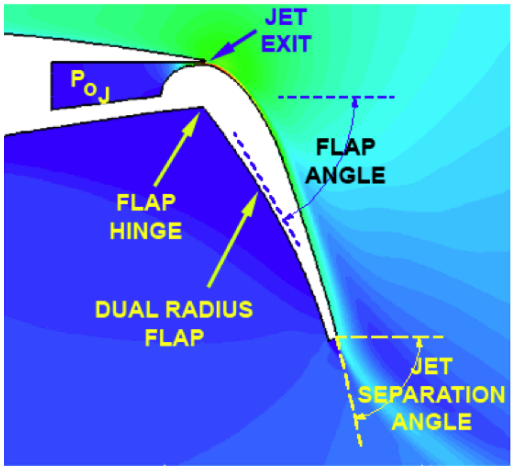

Figure 3. Circulation control blowing slot nomenclature.

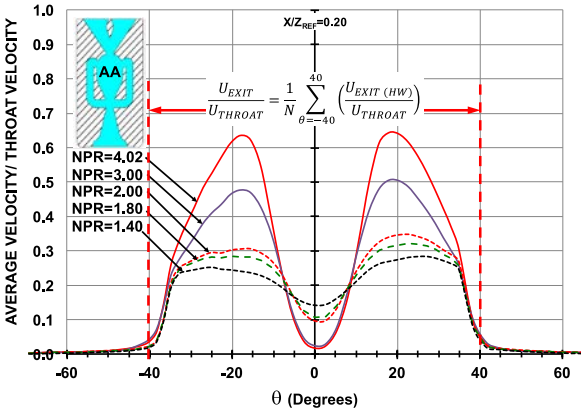

(a) THROAT: 0.080”x0.080” EXIT Y: 0.040”, θ=±35.5º

Figure 4. Exit performance of a single sweeping jet actuator using hot-wire anemometry.

Aerial Photo of NTF complex

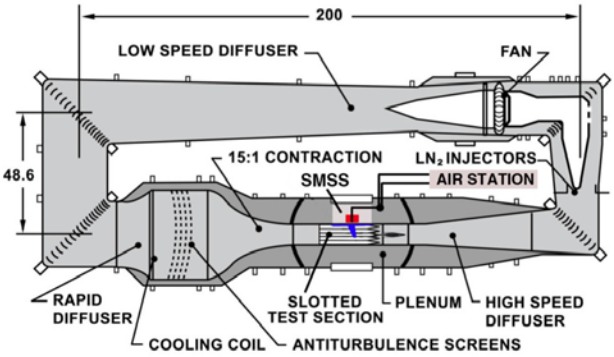

Sketch of NTF highlighting semispan configuration

Figure 5. The National Transonic Facility (NTF).

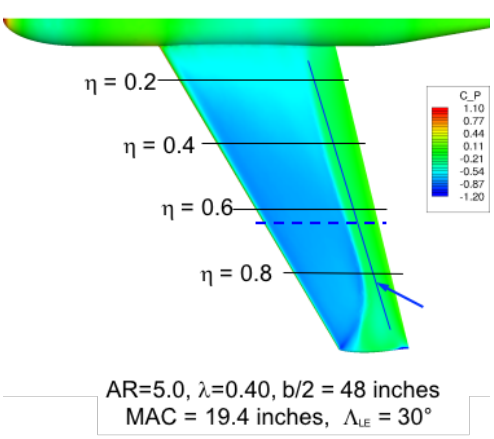

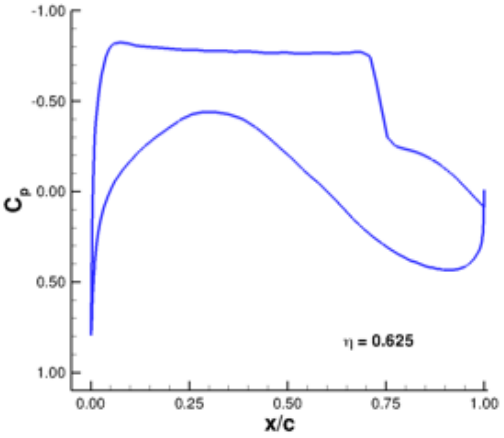

Figure 6. FAST-MAC baseline characteristics.

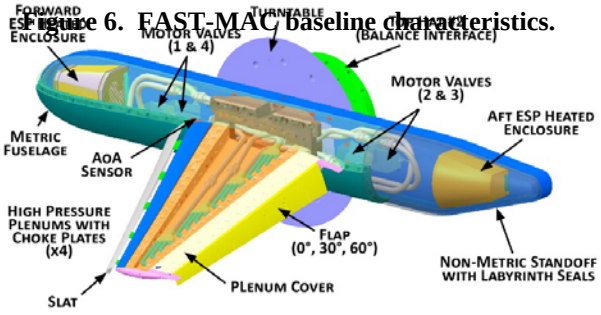

Figure 7. Cutaway view of the FAST-MAC model in high-lift mode.

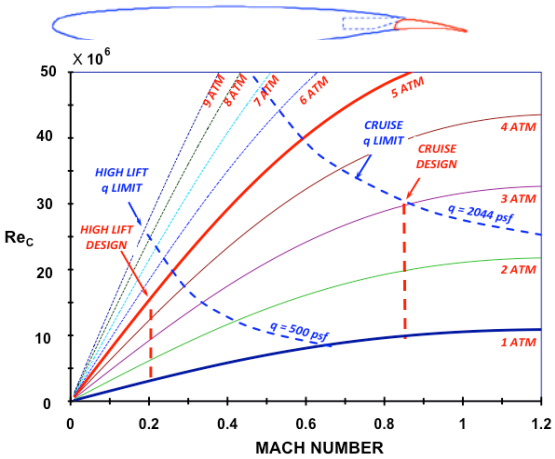

Figure 8. NTF operating envelope for FAST-MAC, To=-50°F, MAC=19.4 inches.

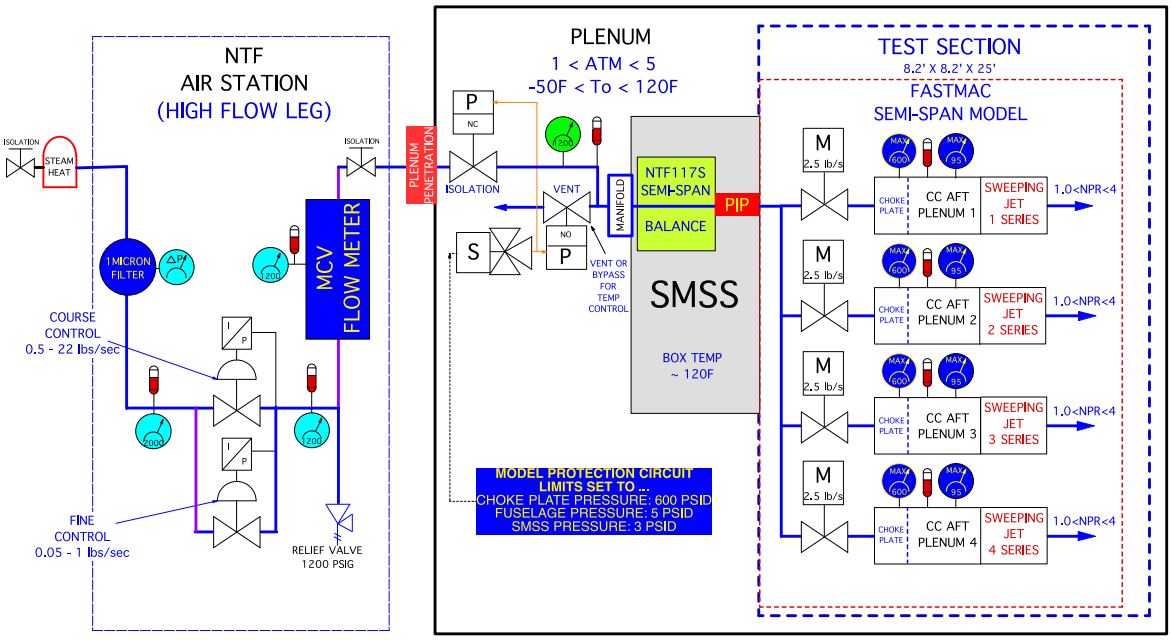

Figure 9. Schematic of the air delivery system for FAST-MAC with sweeping jets.

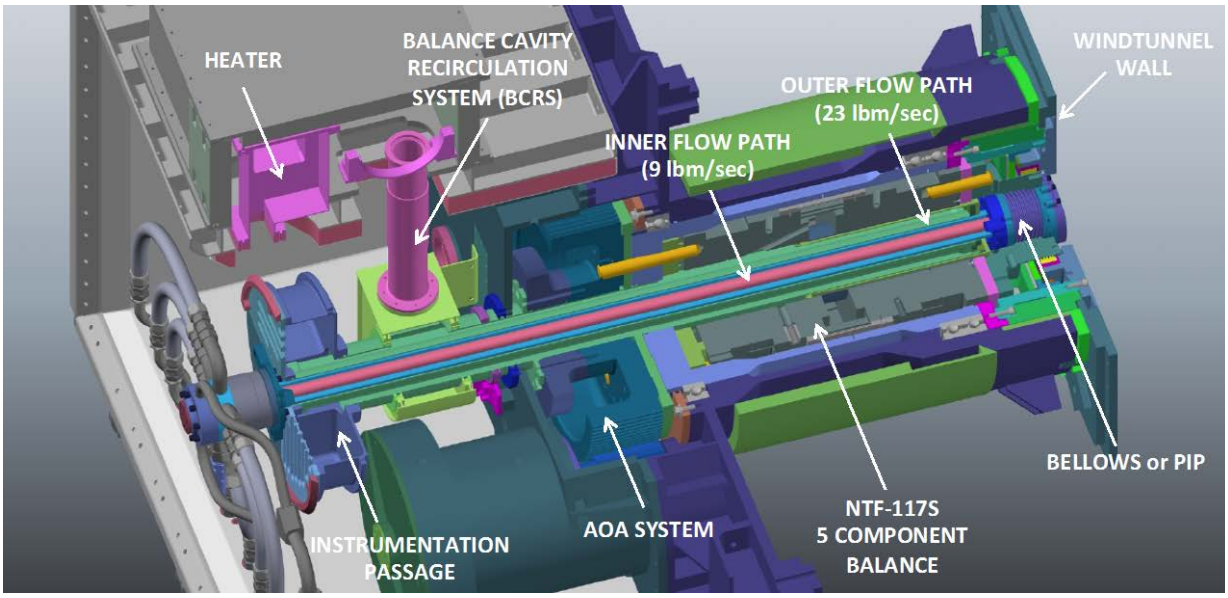

Figure 10. Cutaway sketch of the NTF SMSS highlighting the balance and co-annular flow path.

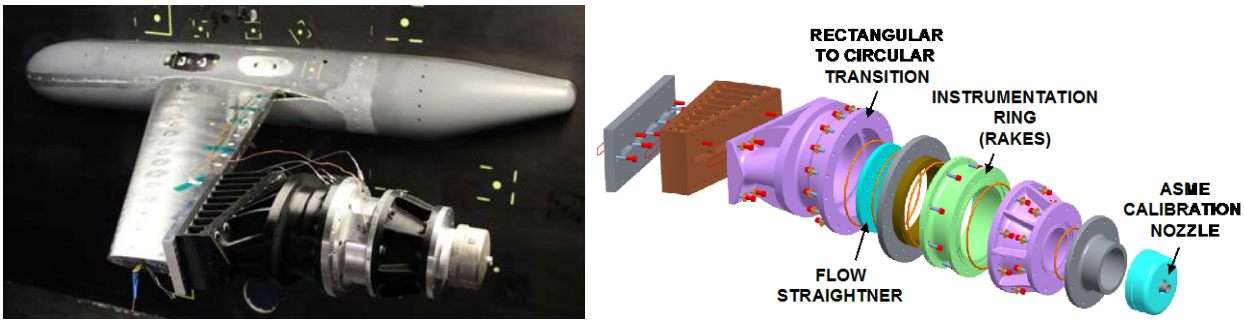

Figure 11. Axial thrust calibration nozzle configuration.

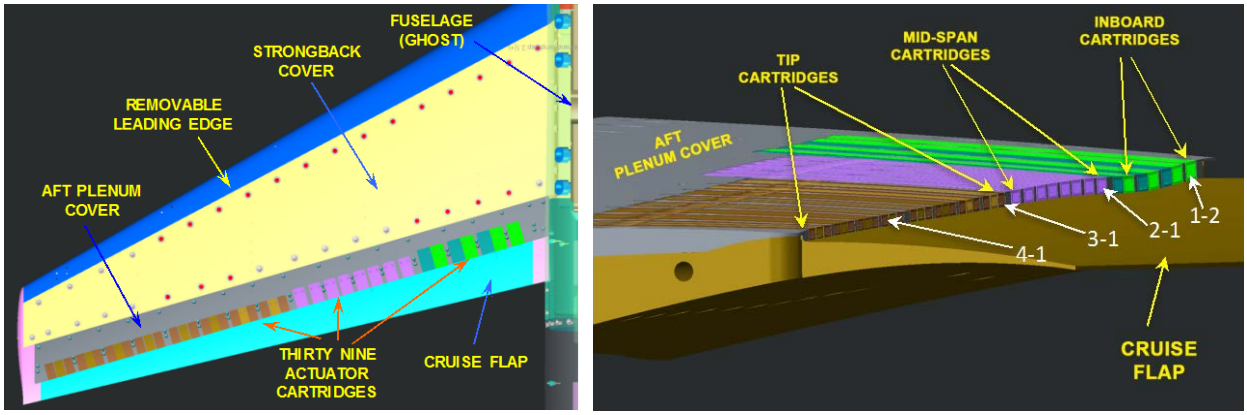

(a) Orientation of the actuator cartridges **(b) Side view of the sweeping jet actuator cartridges**

Figure 12. FAST-MAC actuator locations.

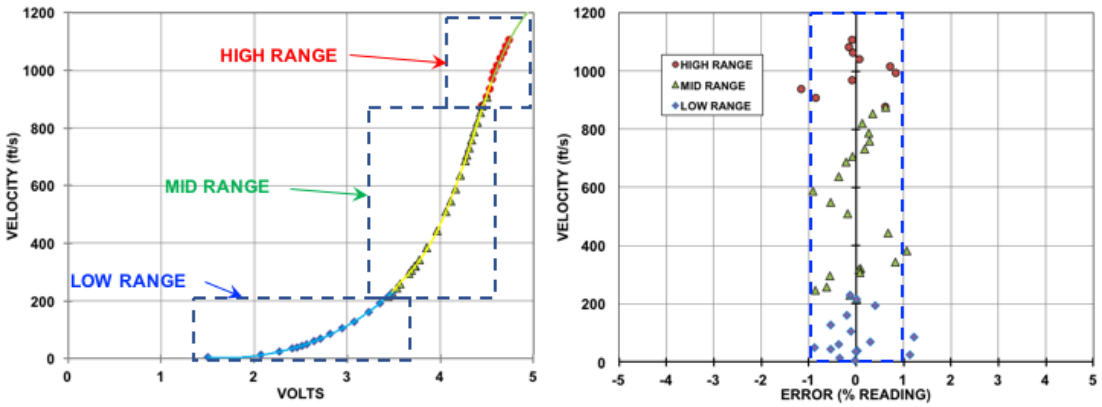

Figure 13. Hot-wire calibration and repeatability for a multi-range polynomial fit.

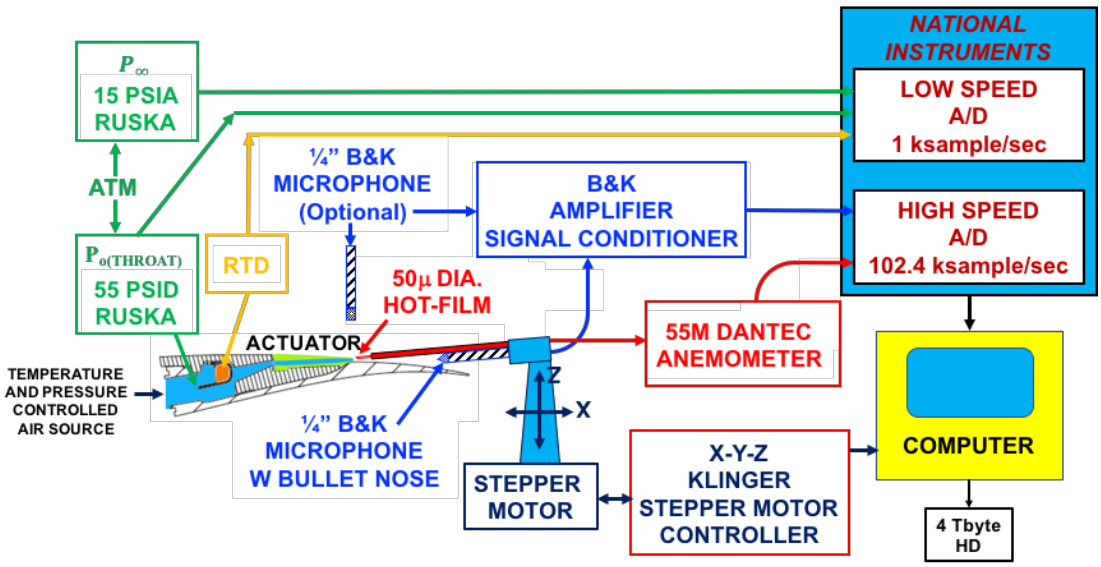

Figure 14. Block diagram of NTF Model Prep Area data acquisition system.

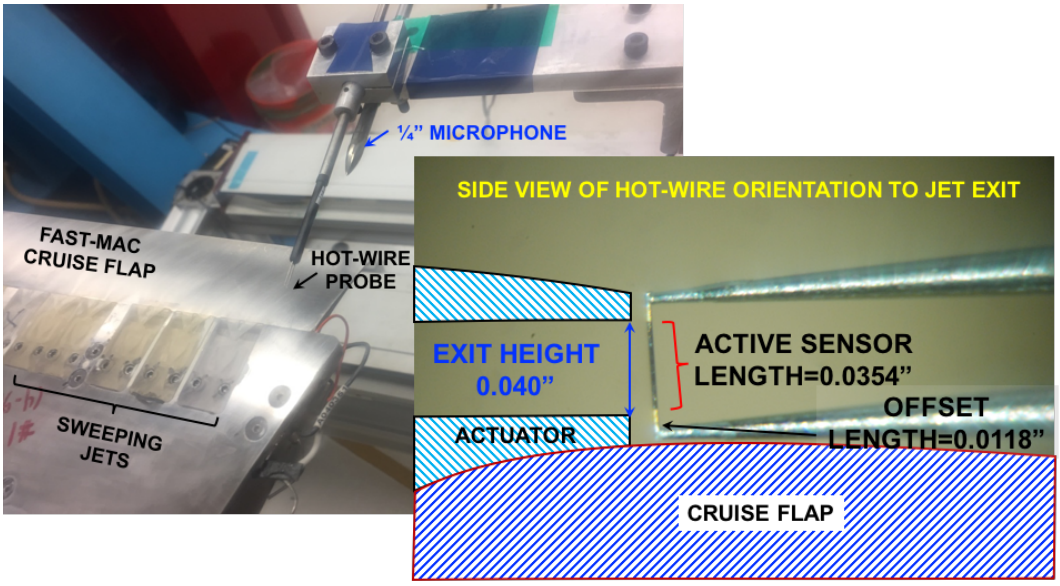

Figure 15. Hot-wire and microphone setup for distributed actuator measurements.

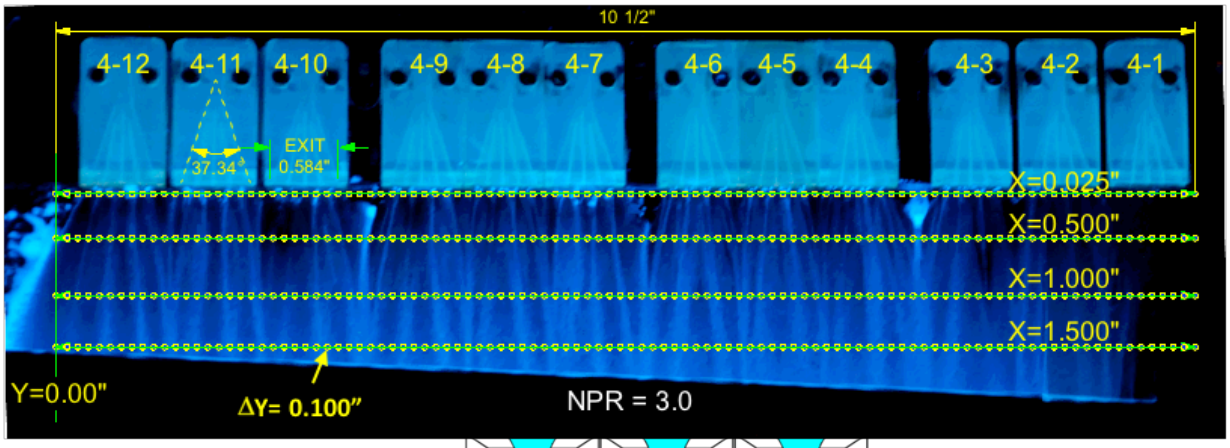

Figure 16. Hot-wire measurement locations for flow path 4 shown on top of surface oil flow visualization.

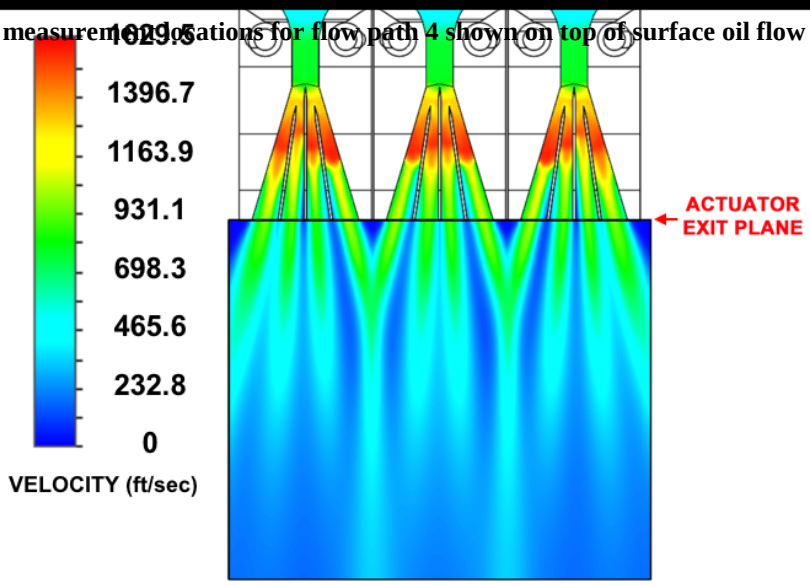

Figure 17. CFD velocity characteristics for the discrete steady actuator geometry in quiescent air, *NPR*=3.0.

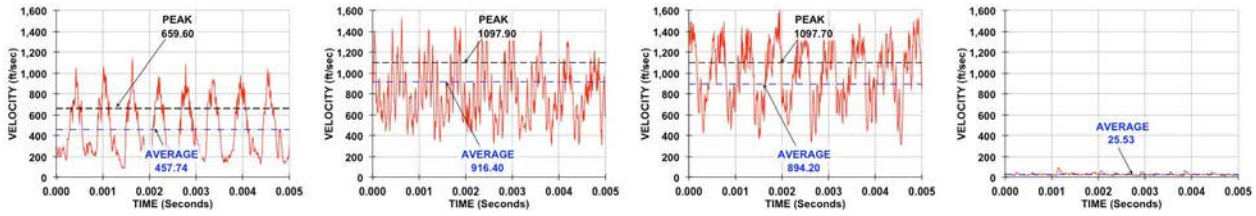

(a) (θ = 31.2º) **(b) (θ = 18.0º)** **(c) (θ = 15.6º)** **(d) (θ = 0.0º)**

Figure 18. Time history example of sweeping jet at different spanwise locations, *NPR*=4.0, X/h=0.625.

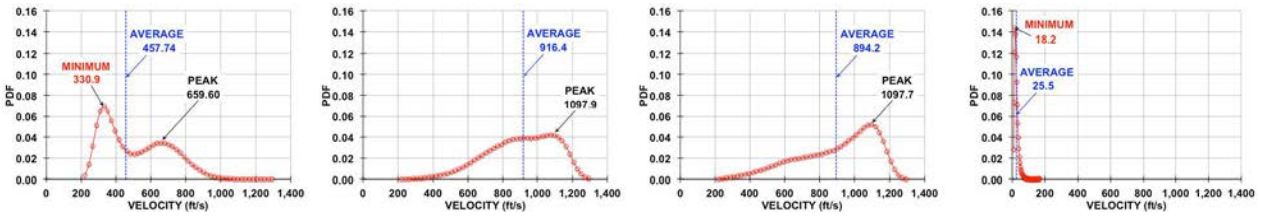

(a) (θ = 31.2º) **(b) (θ = 18.0º)** **(c) (θ = 15.6º)** **(d) (θ = 0.0º)**

Figure 19. Example of PDF of sweeping jet at different spanwise locations, *NPR*=4.0, *X/h*=0.625.

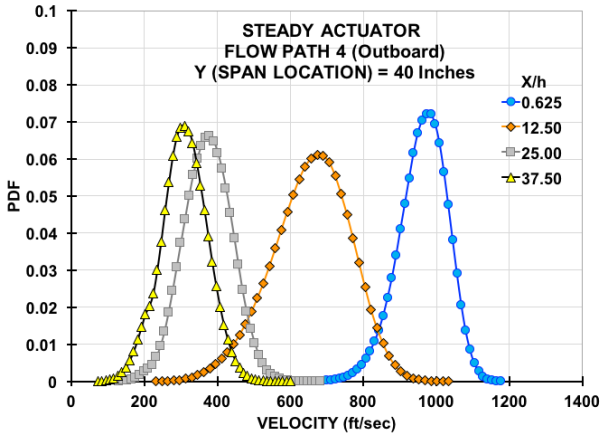

Figure 20. Hot-wire velocity PDF for steady actuator at different streamwise locations, Actuator 4-10, *NPR*=3.0.

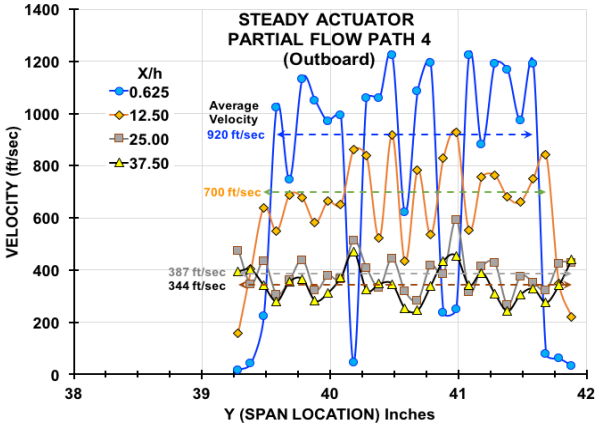

Figure 21. Steady actuator partial span velocity profiles, Actuators 4-10 thru 4-12, *NPR*=3.0

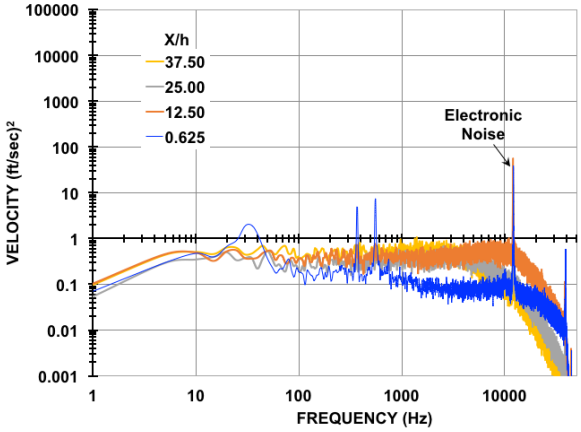

Figure 22. Hot-wire velocity spectra for steady actuator at different streamwise locations. Actuator 4-10, *NPR*=3.0.

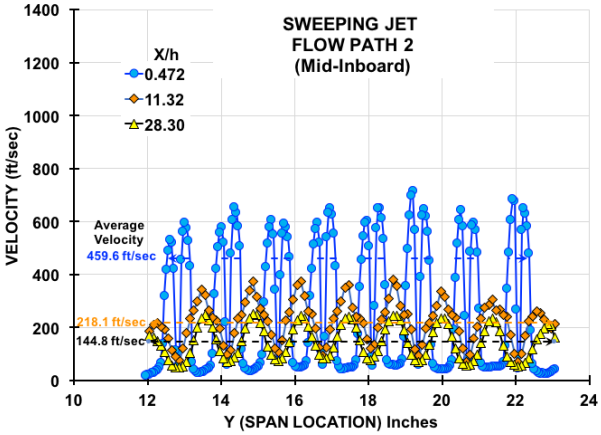

Figure 23. Sweeping jet actuator velocity profiles, Actuators 2-1 thru 2-8, *NPR*=3.0

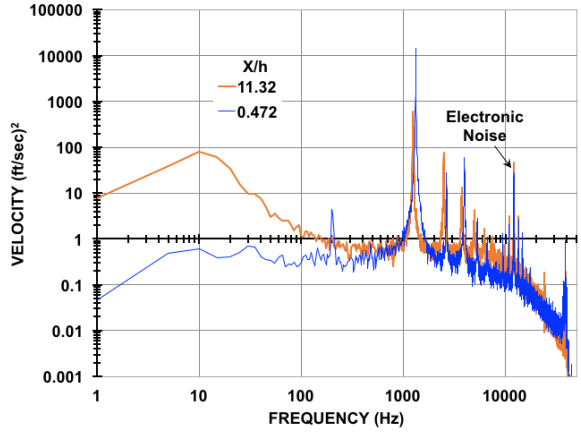

Figure 24. Hot-wire velocity spectra for sweeping jet, Actuator 2-7, *NPR*=3.0.

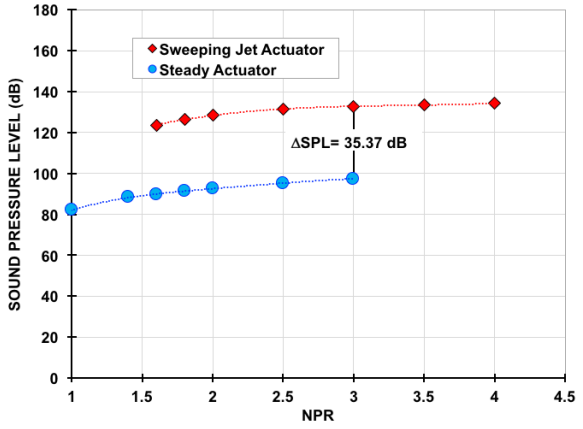

Figure 25. Comparison of SPL for steady actuators and sweeping jet actuators (*Z/h*=27.5).

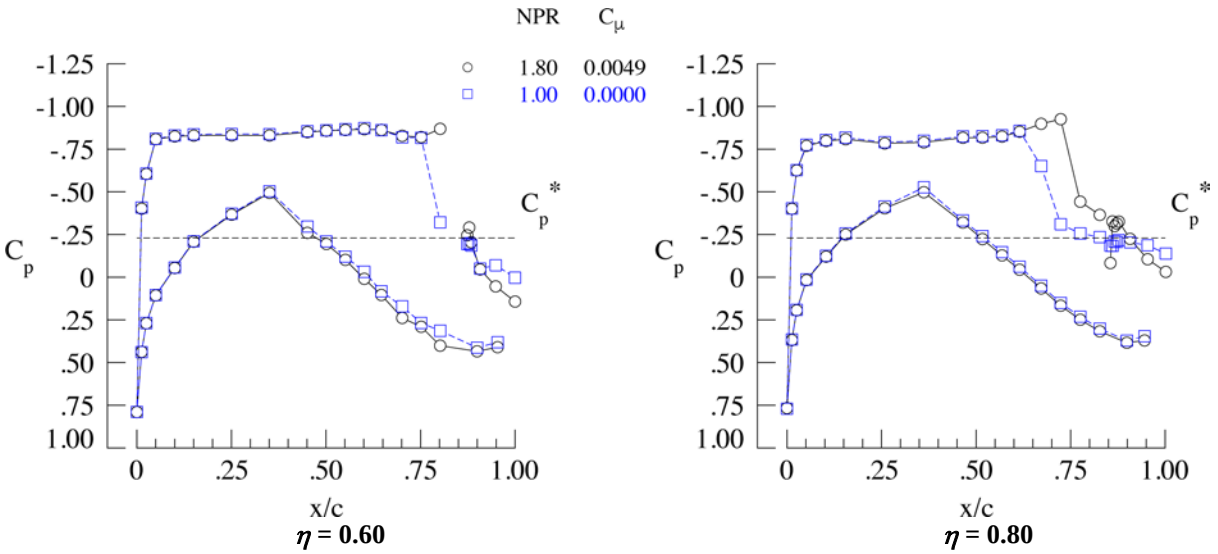

Figure 26. Effect of fullspan steady blowing on wing pressures at off-design conditions, 0° flap deflection, Mach=0.88, α=3°, Re_c=30x10^6.

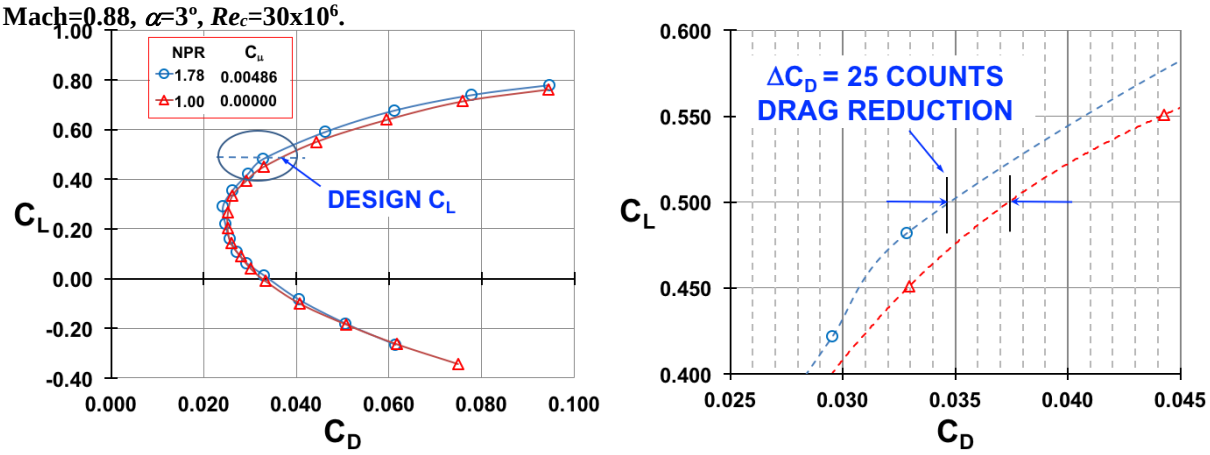

a. ***Polar*** b. ***Zoomed on Design C_L***

Figure 27. Drag improvement using fullspan steady blowing, 0° flap deflection, Mach=0.88, α=3°, Re_c=30x10^6.

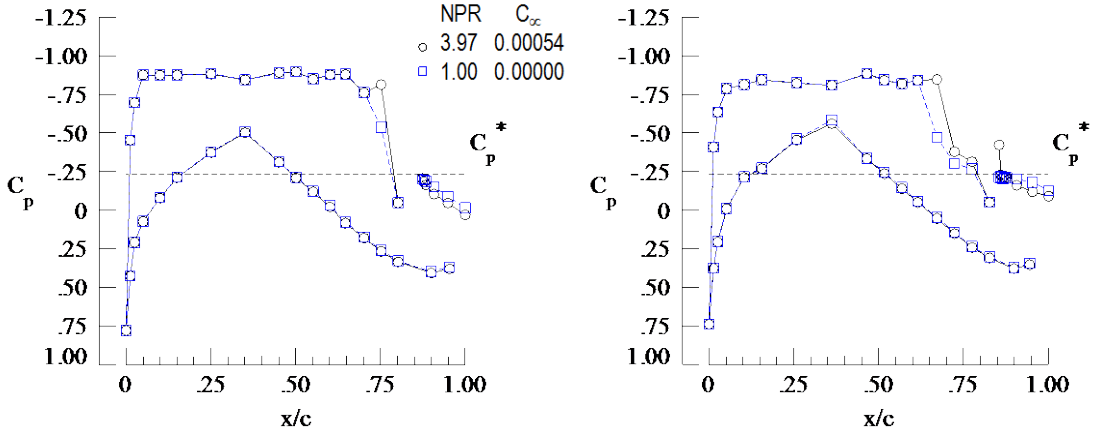

Figure 28. Effect of sweeping jet on wing pressures at off-design conditions, 0° flap deflection, Mach=0.88, α=3°, Re_c=15x10^6.

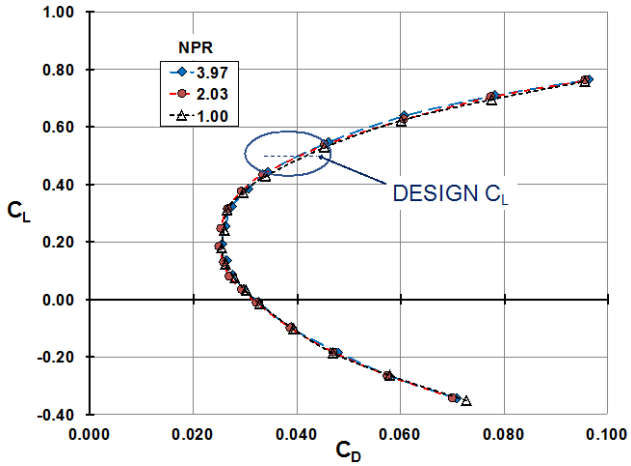

b. *Polar*

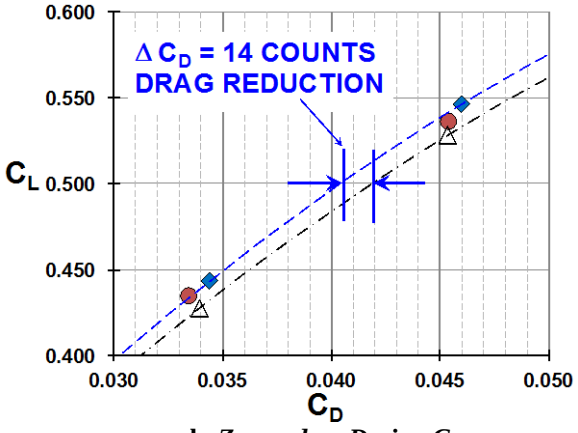

b. *Zoomed on Design C_L*

Figure 29. Off-design drag polar using sweeping jet actuator, Mach=0.88, α=3°, Re_c=15x10^6.

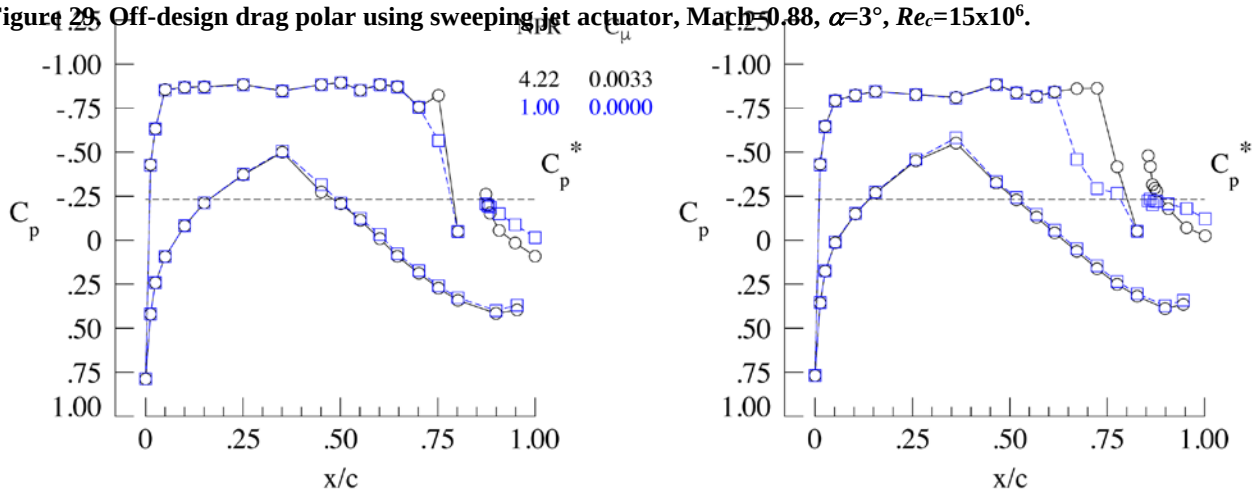

η = 0.60 η = 0.80

Figure 30. Effect of discrete steady jet actuator on wing pressures, Mach=0.88, α=3°, Re_c=15x10^6.

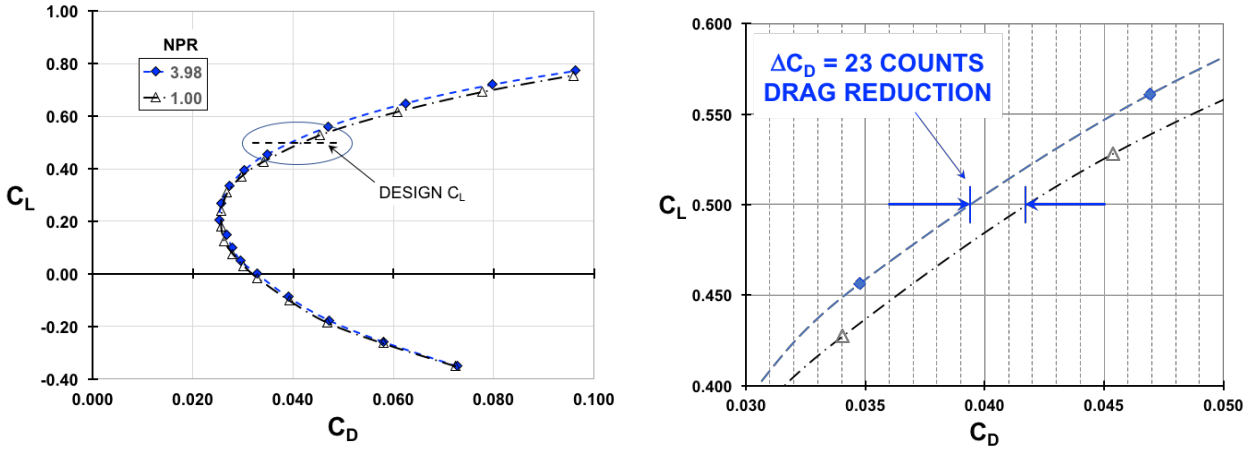

a. *Polar* b. *Zoomed on Design C_L*

Figure 31. Effect of discrete steady jet actuator on lift and drag coefficients, Mach=0.88, α=3°, Re_c=15x10^6.

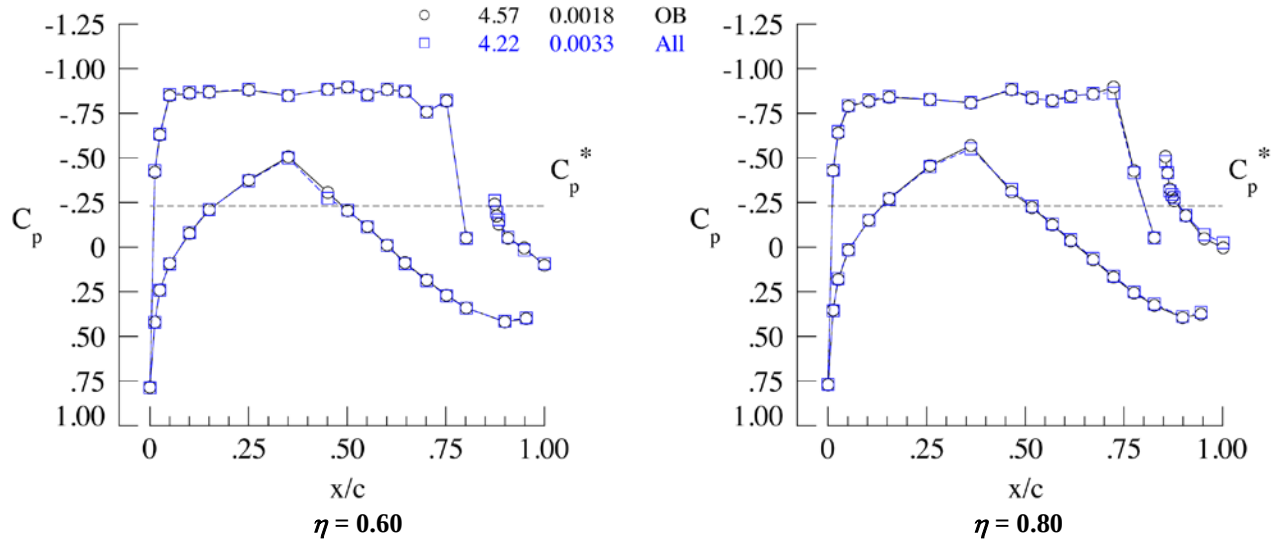

η = 0.60 **η = 0.80**

Figure 32. Effect of spanwise variation of discrete steady blowing on wing pressures, Mach=0.88, α=3°, Re_c=15x10^6.

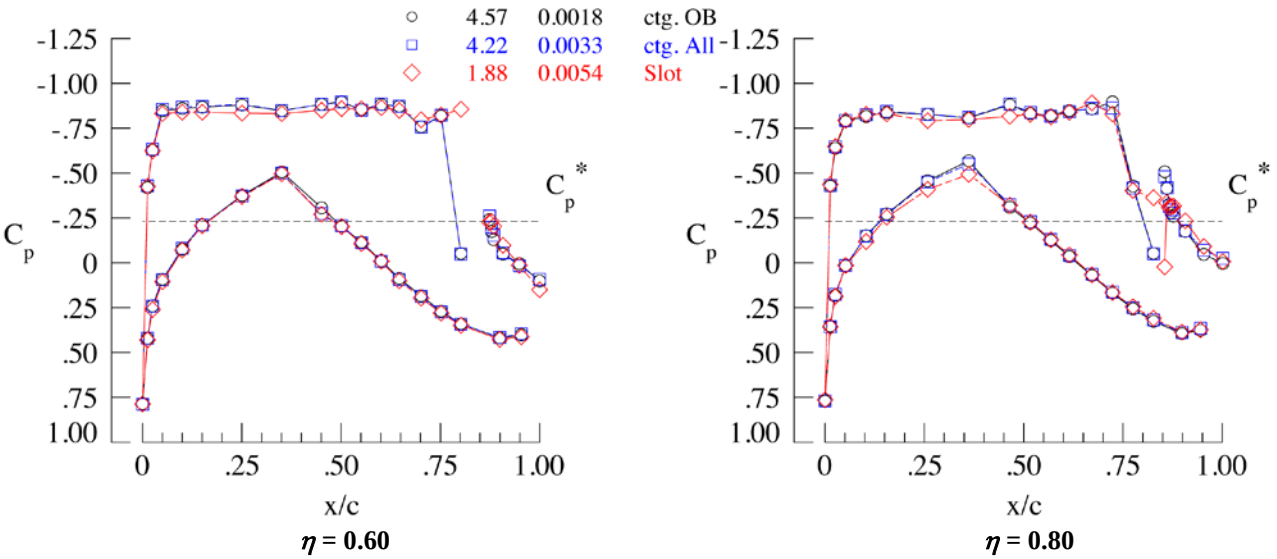

η = 0.60 **η = 0.80**

Figure 33. Effect of steady blowing configurations on wing pressures, Mach=0.88, α=3°, Re_c=15x10^6.

References

[1] Jones, G.S., Joslin, R.D., "Proceedings of the 2004 NASA/ONR Circulation Control Workshop", NASA/CP-2005-213509, June 2005.

[2] Jameson, K.K, Marshal, D.D., Golden, R., Paciano, E., Englar, R.J., Gaeta, R.J., Paterson, J. Mason, D., "Part1: The Wind Tunnel Model Design and Fabrication of Cal Poly' AMELIA 10 Foot Span Hybrid Wing-Body Low Noise CESTOL Aircraft," AIAA Paper 2011-1306, January 2011.

[3] Zeune, C.H., "An Overview of the Air Force's Speed Agile Concept Demonstration Program," AIAA Paper 2013-1097, January 2013.

[4] Barberie, F.J., Wick, A.T., Hooker, J.R., Zeune, C.H., "Low Speed Powered Lift Testing of a Transonic Cruise Eficient STOL Military Transport,", AIAA Paper 2013-1099, January 2013.

[5] Harrison, N.A., Vassberg, J.C., DeHann, M.A., Gea, L.M., "The Design and Test of a Swept Wing Upper Surface Blowing (USB) Concept," AIAA paper 2013-1102, January 2013.

[6] Milholen II, W.E., Jones, G.S., and Cagle, C.M., "NASA High-Reynolds Number Circulation Control Research - Overview of CFD and Planned Experiments (Invited)", AIAA Paper 2010-344, January 2010.

[7] Milholen, W.E., Jones, G.S., Chan, D.T., and Goodliff, S.L., "High-Reynolds Number Circulation Control Testing the National Transonic Facility (Invited)", AIAA paper 2012-0103, January 2012.

[8] Jones, G.S., Milholen II, W.E., Chan, D.T., Melton, L.P., Anders, S.G., Allan., B.G., Carter, M.B., Capone, F.J., and Goodliff, S.L., "Development of the Circulation Control Flow Scheme used in the Semi-Span FAST-MAC Model", AIAA Paper 2013-3048, June 2013.

[9] Wahls, R.A., "The National Transonic Facility: A Research Retrospective (Invited)," AIAA Paper 2001-16587, January 2001.

[10] Frink, N. T., "Tetrahedral Unstructured Navier-Stokes Method for Turbulent Flows," *AIAA Journal*, Vol. 36, No. 11, November 1998, pp. 1975-1982.

[11] Campbell, Richard L, "Efficient Viscous Design of Realistic Aircraft Configurations (Invited)", AIAA Paper 98-2539, June 1998.

[12] Gatlin, G.M, Tomek, W.G., Payne, F.M., and Griffiths, R.C., "Recent Improvements in Semispan Testing at the National Transonic Facility (Invited)", AIAA Paper 2006-508, January 2006.

[13] Jones, G.S., Milholen II, W.E., Goodliff, S.L., "Development of the Dual Aerodynamic Nozzle Model for the NTF Semispan Model Support System," AIAA Paper 2011- 3170, June 2011.

[14] Mikkelsen, K.L., Olstad, S.J.,"Airflow Calibrations of NASA Langley Research Center Multiple Critical Venturi (MCV) Assemblies," FluiDyne Report 1835, June 1992.

[15] Lynn, K.C., "Development of the NTF-117S Semispan Balance", AIAA Paper 2010-4542, June 2010.

[16] Lynn, K.C., Rhew, R.D., Acheson, M.J., Jones, G.S., Milholen II, W.E., Goodliff, S.L., "High Reynolds Number Active Blowing Semispan Measurement System Development," AIAA Paper 2012-3318, June 2012.

[17] Goodliff, S.L., Jones, G.S., Balakrishna, S., Chan, D.T., Milholen, II, W.E., Butler, D., Cagle, C.M., "Force Measurement Improvements to the National Transonic Facility Sidewall Model Support System," AIAA Paper 2016-0648, January 2016.

[18] Chan, D.T., Hooker, J.R., Wick, A.T., Plumley, R.W., Zeune, C.H., Ol, M.V., Demoss, J.A., "Transonic Semispan Aerodynamic Testing of the Hybrid Wing Body with Over Wing Nacelles in the National Transonic Facility," AIAA Paper 2017-0098, January 2017.

[19] Chan, D.T., Milholen II, W.E., Jones, G.S., Goodliff, S.G., "Thrust Removal Methodology for the FAST-MAC Circulation Control Model Tested in the National Transonic Facility," AIAA Paper 2014-2402.

[20] Jones, G.S., Milholen II, W.E., Fell, J.S., Webb, S.R., Cagle, C.M., "Using Computational Fluid Dynamics and Experiments to Design Sweeping Jets for High Reynolds Number Cruise Configurations", AIAA Paper 2016-3311.

[21] Chan, D.T., Jones, G.S., Milholen II, W.E., Goodliff, S.G., "Transonic Drag Reduction Through Trailing-Edge Blowing on the FAST-MAC Circulation Control Model," AIAA Paper 2017-3246, June 2017

[22] Jones, G.S., Milholen II, W.E., Chan, D.T., Goodliff, S.G., "A Sweeping Jet Application on a High Reynolds Number Semi-Span Supercritical Wing Configuration", AIAA Paper 2017-3044, June 2017.